

# Startup Control Optimization of He-Xe Cooled Space Nuclear Reactors Using a System Analysis Program

Chengyuan Li<sup>a,b</sup>, Leran Guo<sup>a</sup>, Shanfang Huang<sup>a,\*</sup>, Jian Deng<sup>b</sup>, Jiahe Shang<sup>a</sup>

<sup>a</sup> Department of Engineering Physics, Tsinghua University, Beijing, 100084, China

<sup>b</sup> National Key Laboratory of Nuclear Reactor Technology, Nuclear Power Institute of China, Chengdu, 610213, China

\* Corresponding author: [sfhuang@mail.tsinghua.edu.cn](mailto:sfhuang@mail.tsinghua.edu.cn)

## Highlights

1. Proposed a framework to optimize startup control sequences
2. Developed a system analysis code using non-ideal gas and multi-channel core model
3. Verified system analysis code under steady state and startup transient
4. Optimized control reduced startup time by 1260 s in power and 1980 s in temperature

**Abstract:** In recent years, achieving autonomous control in nuclear reactor operations has become pivotal for the effectiveness of Space Nuclear Power Systems (SNPS). However, compared to power control, the startup control of SNPS remains underexplored. This study introduces a multi-objective optimization framework aimed at enhancing startup control, leveraging a system level analysis program to simulate the system's dynamic behavior accurately. The primary contribution of this work is the development and implementation of an optimization framework that significantly reduces startup time and improves control efficiency. Utilizing a non-ideal gas model, a multi-channel core model and the Monte Carlo code RMC employed to calculate temperature reactivity coefficients and neutron kinetics parameters, the system analysis tool ensures precise thermal-dynamic simulations. After insightful comprehension of system dynamics through reactive insertion accidents, the optimization algorithm fine-tunes the control sequences for external reactivity insertion, TAC system shaft speed, and cooling system background temperature. The optimized control strategy achieves threshold power 1260 seconds earlier and turbine inlet temperature 1980 seconds sooner than baseline methods. The findings highlight the potential of the proposed optimization framework to enhance the autonomy and operational efficiency of future SNPS designs.

**Keywords:** Helium-xenon cooling, Closed Brayton Cycle, Non-ideal gas model, Multi-channel core model, Startup control optimization

## 1 Introduction

Deep space exploration missions are becoming increasingly critical in addressing Earth's looming issues such as resource depletion and overpopulation. Missions extending beyond 10 years and requiring power levels exceeding 100 kWe, such as the exploration of Jupiter's icy moons, necessitate advanced power systems. Among these, a nuclear power system with a Closed Brayton Cycle (CBC) and a direct-cycle helium-xenon gas-cooled reactor stands out as an optimal solution[1].

This Space Nuclear Power System (SNPS) benefits from the direct coupling of the power system and reactor core, where helium-xenon gas circulates through the reactor to drive the turbine. The integrated Brayton cycle, using He-Xe gas, delivers higher power levels and superior power-to-mass ratios compared to other space reactors. This design also circumvents the thermal transfer limits of heat pipes and minimizes system weight by eliminating intermediate heat extraction devices[2]. Additionally, the He-Xe gas mixture enhances heat removal efficiency and reduces the compressor mass by decreasing compression work and the number of compressor rotor blade stages[3].

The concept of employing a helium-xenon reactor as a megawatt-class nuclear power source for deep space missions can be traced back to NASA's Prometheus Project, initiated in 2003[4,5]. During the design phase, five schemes were evaluated for a 200 kWe power source with a mission duration of 15-20 years. Among these, the helium-xenon reactor with a direct Brayton cycle was selected for further study.

The reactor concept continued to evolve. In 2009, Russia launched its megawatt-class space transport ship project (Transport and Energy Module, TEM)[6]. The reactor for this project has a power output of 3.5 MWt and a core outlet temperature of 1500 K. It employs four helium-xenon closed Brayton cycles, delivering an output power of 1 MWe with a conversion efficiency of 34%[7,8]. Furthermore, in 2013, the EU initiated the MEGAHIT project, followed by the DEMOCRITOS project for validation[9]. This initiative aims to develop a 1 MWe nuclear electric propulsion spacecraft, capable of delivering 18 tons to Mars and 12 tons to Europa, with a power-to-mass ratio of 20 kg/kWe, thruster specific impulse of 2000-9000 seconds, and a core outlet temperature above 1300 K. The project has designed a direct Brayton cycle

propulsion system, a ground demonstrator, and strategies for in-orbit assembly[9–12]. The next step is orbital validation by 2025[13].

The startup phase is crucial for the operational success of the SNPS. If startup fails, it cannot be repeated, making it imperative to optimize startup control to reduce startup time. Successful startup is essential as power consumption before startup completion is supported by limited-capacity storage batteries. Therefore, predicting dynamic behavior and optimizing the control processes of these systems is vital.

A few control methods have been explored in existing research. Skorlygin[14] introduced a startup optimization method that measures temperature, calculates the critical position of the control rod, and adjusts it using bidirectional movement to achieve the desired startup time. Prikot et al.[15] enhanced the control algorithm of the TOPAZ-II space nuclear power system, achieving precise power control and protecting the thermionic emitter from overheating during startup, thus improving startup performance and stability. Zeng et al.[16] used a nonlinear model and fuzzy PID controller to optimize reactivity introduction, power steps, and load-following control of TOPAZ-II. Ma et al.[17] analyzed the startup control of a megawatt heat pipe reactor coupled to a close brayton cycle. However, the strategies are mainly dependent on expert knowledge. Further information on modeling and control issues in nuclear power systems is available in reference[18].

Optimizing the control needs a system analysis program, but such tools integrating the core and power system is limited. McCann et al.[19] used RELAP-3D to simulate a CBC coupled nuclear reactor, but the transient behavior was not verified. EI-Genk et al.[20] demonstrated the transient process of the S4 reactor coupled with the CBC, but the core modeling lacked detail and did not account for radial thermal-hydraulic variations. Wang et al.[21] utilized a radial multi-channel reactor model in their system analysis but did not address assumptions about gas properties. Geng et al. [22] constructed an analysis tool, but the core model was considered lumped. Ma et al.[23] analyzed the startup performance of the SNPS with multiple Brayton loops, comparing different startup schemes and the impact of space environment temperature, yet their core description was simplified, and neutron dynamics parameters were unspecified.

This study will first develop a toolset for modeling the closed Brayton cycle reactor system. The non-ideal gas properties of helium-xenon mixtures will be modeled, along with a multi-channel reactor thermal-hydraulic model. Turbomachinery, regenerator, and cooler models within a closed Brayton cycle will also be developed.

The Monte Carlo program RMC will be utilized to obtain temperature reactivity coefficients and neutron kinetic parameters. Furthermore, an evolution-based control optimization framework will be employed to optimize the startup control sequence, aiming to reduce startup time. The workflow of this paper is shown in Figure 1.

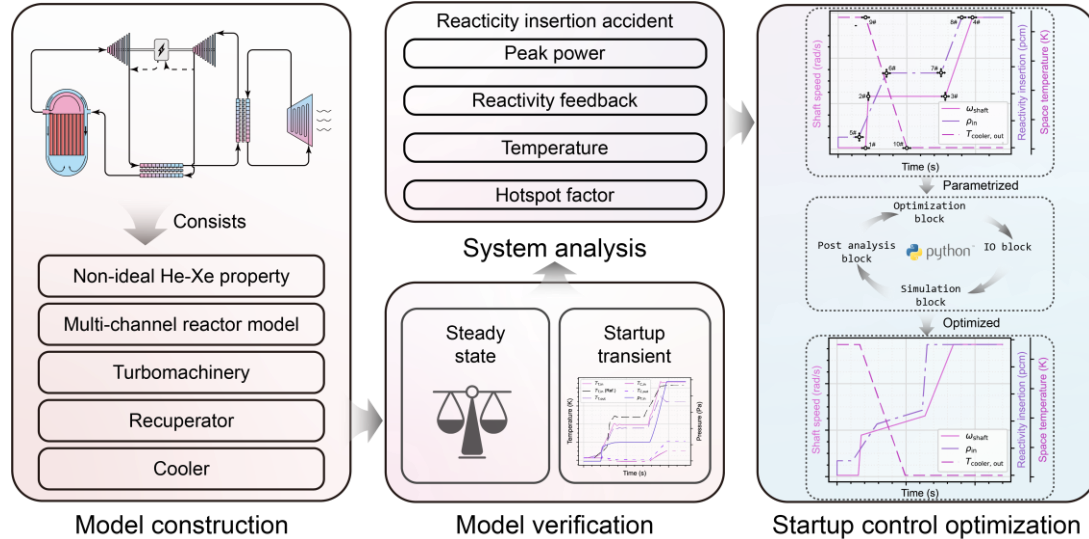


Figure 1 Overview of the workflow proposed in this paper

The rest of this paper is structured as follows: Chapter 2 details the optimization framework of control optimization and the modeling of the reactor system. Chapter 3 verifies the model with steady-state and startup transient. Chapter 4 analyzes reactivity insertion accidents and shows results of startup control optimization. Chapter 5 concludes the study and discusses future implications.

## 2 Methodology

### 2.1 Framework for optimizing the control

There are two methods for optimizing the startup process of space nuclear power systems. The first method involves identifying the controlled variables, dividing fixed time intervals, and utilizing heuristic algorithms or reinforcement learning to optimize the sequence of control variables without external intervention. This approach has the potential for high performance but requires extensive search and is time-consuming. The second method is based on expert knowledge, where adjustments are made at critical control points and constraints are added before optimization. This method has a smaller search space and incorporates expert experience, making it more practical for engineering applications, even though the results may not be globally optimal. Given

the focus of this paper on engineering contributions, the latter approach is used.

The first task is the parameterization of the control sequence. The startup process of the SNPS can be divided into five stages[31]. At each stage, control variables must reach different set points at specific times. Therefore, the magnitude and timing of these set points can be parameterized. Expert knowledge is used to constrain the upper and lower limits of these parameters.

Secondly, define the performance metrics for optimization. For the goal of faster startup, monitor the time at which key system parameters exceed specific thresholds. Use this time as a measure of control performance, and select optimal parameters based on improvements in this metric.

Lastly, the implementation of the algorithms is discussed. For single-objective optimization, algorithms such as Differential Evolution[32], CMA-ES[33], and ISRES[34] can be considered. For optimizing 2 to 3 objectives simultaneously, NSGA-II[35], R-NSGA-II[36], and MOEA/D[37] are suitable choices. For scenarios involving more than three objectives, NSGA-III[38], U-NSGA-III[39], and R-NSGA-III[40] can be utilized.

During the optimization process, it is crucial to consider the coupling between the optimization algorithm and the simulation program. This paper proposes an optimization framework consisting of four modules: IO module, simulation module, post-processing module, and optimization algorithm module. The optimization module controls the overall optimization process. The activity diagram for this framework is shown in Figure 2.

IO module writes the control sequence files to the project directory and saves the data to disk. Simulation module uses files to perform simulations with any simulation software, obtaining changes in all variables for the current generation. Post-processing Module receives variables and calculates the performance metrics. Optimization algorithm module employs single or multi-objective optimization algorithms to define a multi-objective optimization problem based on these metrics and generates the control sequences for the current generation.

In each iteration, the optimization module generates new control sequences, which the IO module saves for the next simulation. This iterative process continues until the optimal control sequence is achieved, ultimately yielding the optimization results.

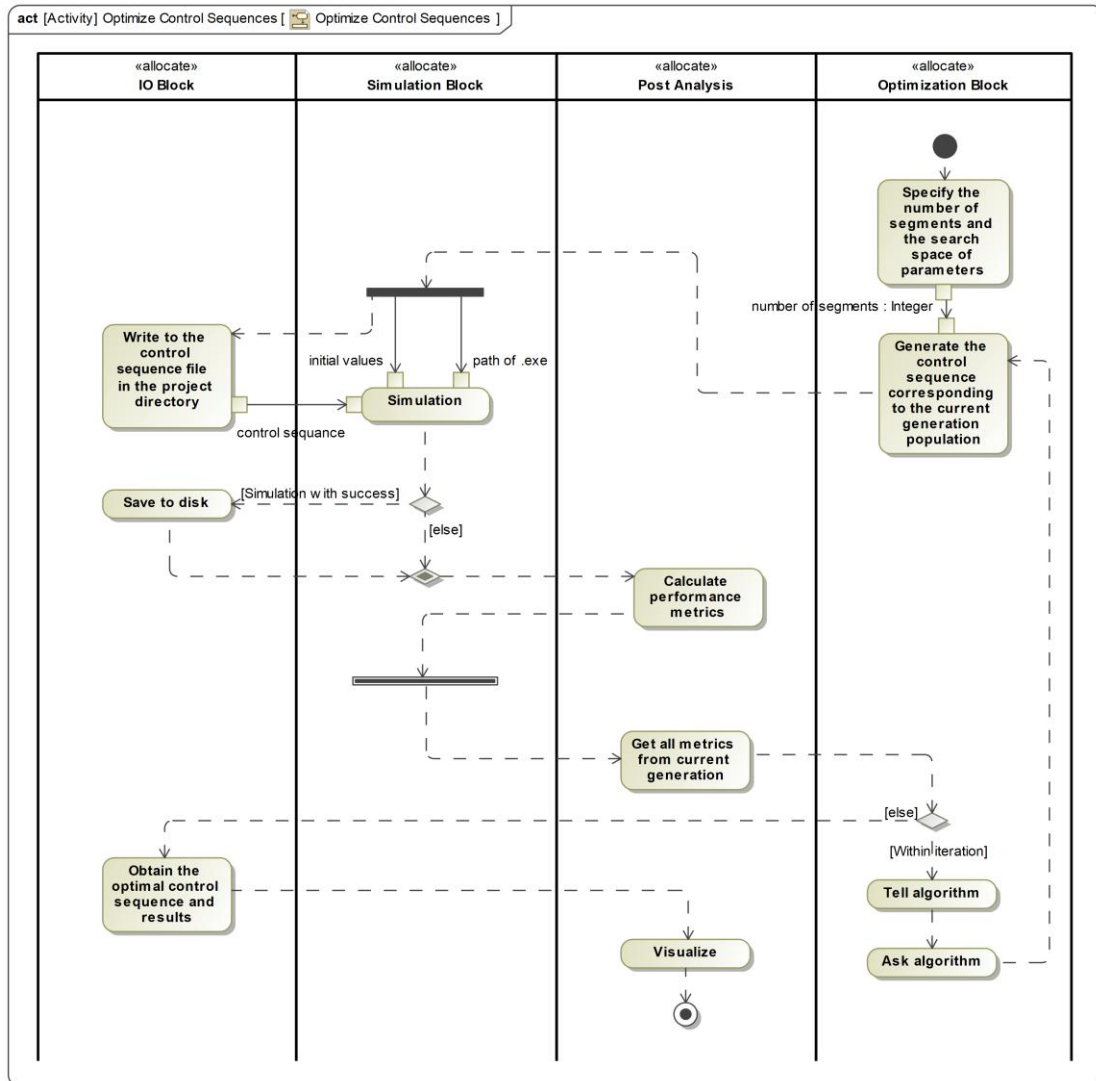


Figure 2 The framework for parameterization and optimization control sequence

## 2.2 Modeling of the CBC nuclear reactor system

The helium-xenon cooled closed Brayton cycle nuclear reactor system efficiently converts energy through thermodynamic cycles. The helium-xenon gas mixture is compressed, raising its temperature and pressure. Preheated in the regenerator, the gas enters the reactor core, reaching high temperatures. It then expands in the turbine, driving the generator to produce electricity. The expanded gas releases heat in the regenerator and is further cooled in the cooler before returning to the compressor, completing the cycle. Such process is depicted in Figure 3. The block definition diagram reflecting the entities and relationships of the system is shown in Figure 4.

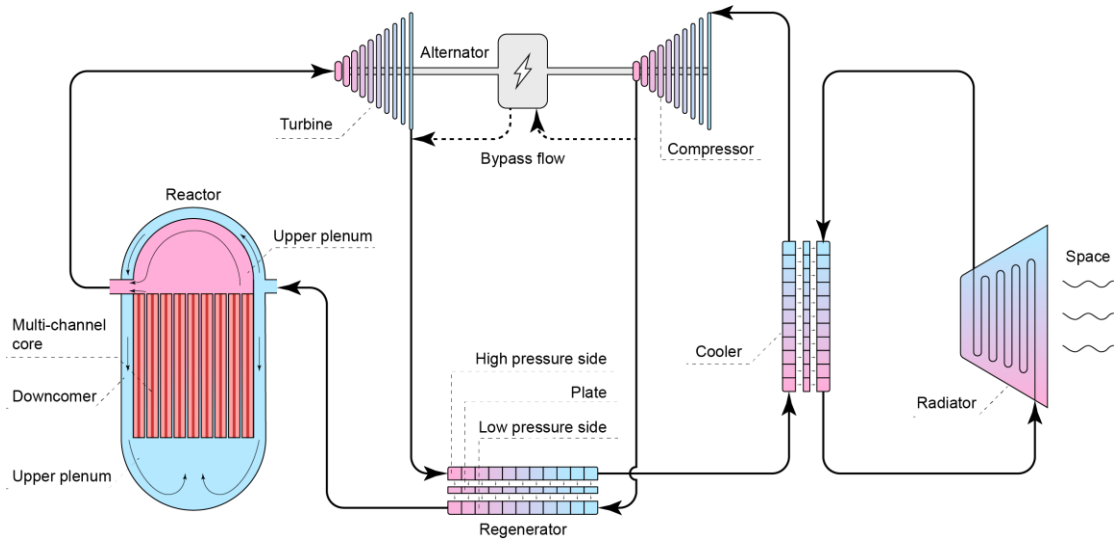


Figure 3 Closed Brayton Cycle reactor system schematic diagram

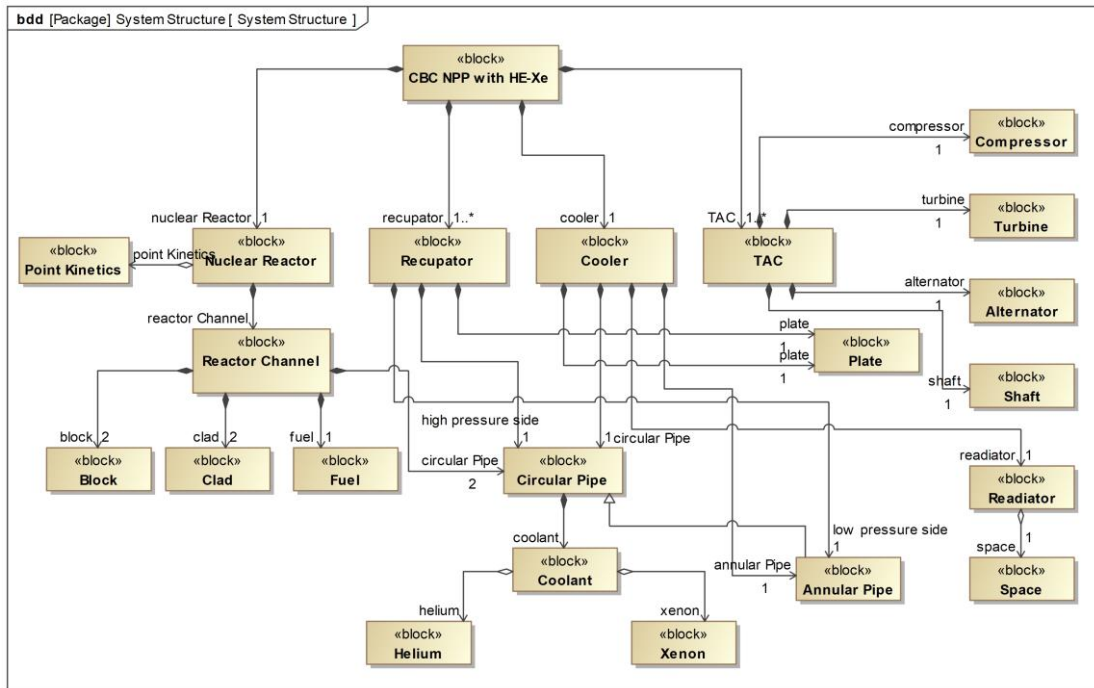


Figure 4 Block definition diagram of closed Brayton Cycle reactor system

### 2.2.1 Non-ideal properties of Helium-Xenon mixture

The ideal gas model assumes no intermolecular forces and negligible molecular volume. However, in a helium-xenon mixture, xenon's larger molecular volume and significant intermolecular forces invalidate these assumptions. Non-ideal effects in such mixtures are significantly influenced by xenon proportion, temperature, and pressure, especially at low temperatures, high pressures, and high xenon concentrations. Therefore, it is crucial to consider non-ideal gas effects and select an appropriate equation of state for accurate analysis.

The density calculation utilizes the Virial Equation combined with semi-empirical relationships[24]. This approach has the advantage of accounting for temperature and pressure effects, making it suitable for a wide range of temperature and pressure conditions. However, its accuracy decreases near the critical point. Given that the operating conditions are far from the critical point, this does not negatively impact.

As the molar mass of helium-xenon mixtures increases, the compression factor rises slowly, peaks around 30.34-61.07 g/mol, and then declines, as shown in Figure 5 and Figure 6. Temperature and pressure significantly affect the compression factor; lower temperatures and higher pressures increase deviations from ideal gas behavior. At low temperatures and high molar mass, the density difference between ideal and non-ideal gases is more pronounced, requiring the mixture to be treated as a non-ideal gas for accurate density measurements.

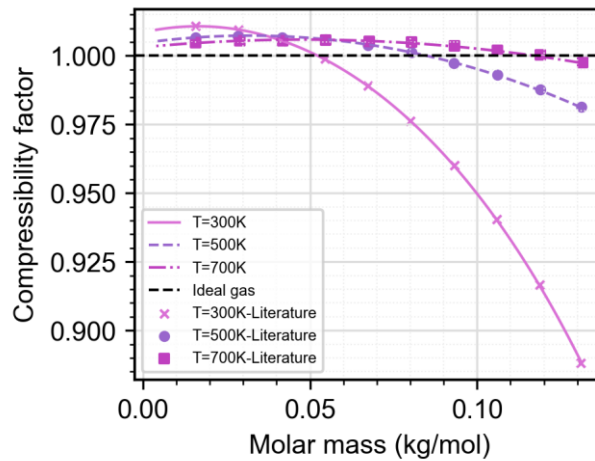


Figure 5 Effect of molar mass on the compression factor at constant pressure (2.0 MPa)

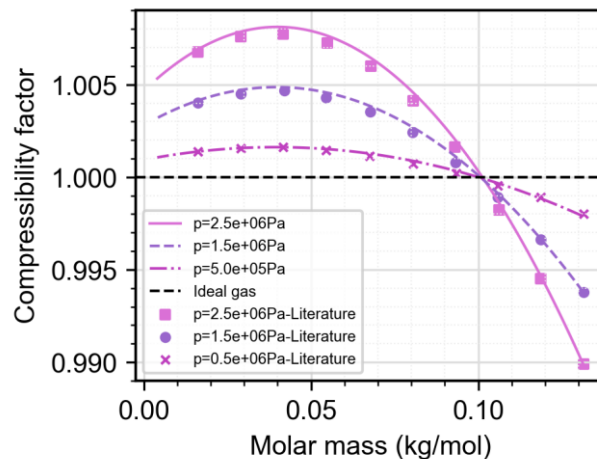


Figure 6 Effect of molar mass on the compression factor at constant temperature (600K)

The calculation of the specific heat capacity at constant pressure is estimated by considering the real gas equation of state, combined with corrections from the virial



equation. This correction ensures that, under pressures ranging from 0.1 to 20 MPa and helium temperatures up to 1500 K, the computed values deviate from the recommended values by the U.S. NIST by no more than 0.1%[25]. The variation of molar heat capacity at constant pressure with molar mass under fixed pressure and temperature conditions is shown in Figure 7 and Figure 8, respectively.

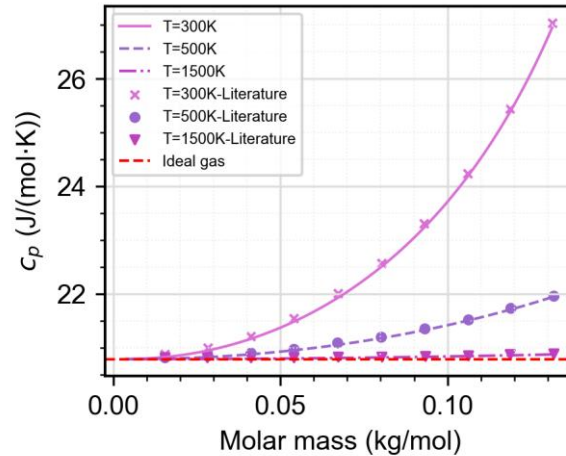


Figure 7 Molar heat capacity at constant pressure varies with molar mass at 2.0 MPa

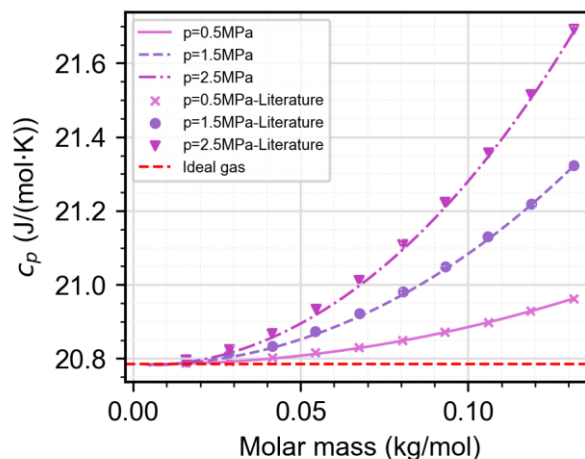


Figure 8 Molar heat capacity at constant pressure varies with molar mass at 600K

Adding xenon increases gas heat capacity, particularly at low temperatures and high pressures. As xenon proportion increases, heat capacity rises, unlike the ideal gas model's prediction. This shows gas composition significantly affects heat capacity under non-ideal conditions. Considering intermolecular interactions improves prediction accuracy in these conditions.

The dynamic viscosity and thermal conductivity of helium-xenon (He-Xe) mixtures were calculated using Hirschfelder's method. Specifically, the viscosity calculation employed Chapman-Enskog theory, which assumes spherical molecules with no internal degrees of freedom. The thermal conductivity calculation incorporated

Singh's third-order correction factor to Hirschfelder's method, accounting for higher-order effects of mass and temperature[26]. Changes in dynamic viscosity and thermal conductivity with gas molar mass are shown in Figure 9 and Figure 10, respectively.

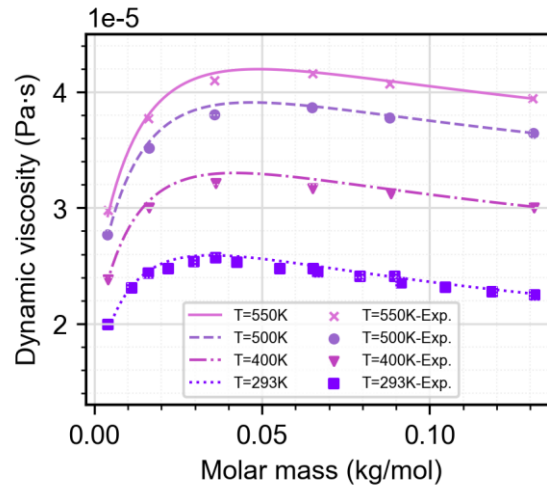


Figure 9 Dynamic viscosity with gas molar mass at different temperatures

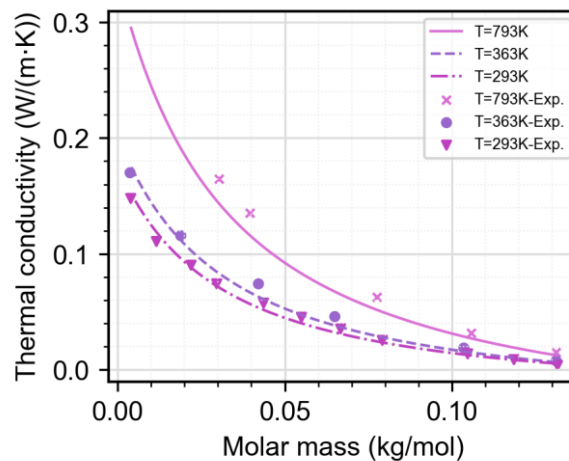


Figure 10 Thermal conductivity with gas molar mass at different temperatures

The data from the figures closely match those in reference[26]. In the temperature range of 400K to 1200K, for helium-xenon mixtures of different molecular weights, the calculated first-order dynamic viscosity values deviate from AiResearch data by no more than 0.51%. The calculated third-order thermal conductivity values deviate from AiResearch data by 2.13% to 4.40%.

## 2.2.2 Reactor model

The reactor model includes a neutron kinetics model and a multi-channel thermal-hydraulic model.

### 2.2.2.1 Neutron kinetics

Neutron kinetics use the point reactor model, with the governing equation as

$$\begin{aligned}\frac{dP_{\text{fiss}}(t)}{dt} &= \frac{\rho(t) - \sum_{i=1}^6 \beta_i}{\Lambda} P_{\text{fiss}}(t) + \sum_{i=1}^6 \lambda_i C_i(t) \\ \frac{dC_i(t)}{dt} &= \frac{\beta_i}{\Lambda} P_{\text{fiss}}(t) - \lambda_i C_i(t) \quad i = 1, 2, \dots, 6 \\ \rho(t) &= \rho_{\text{in}}(t) + \rho_{\text{fuel}}(T_{\text{fuel,avg}}) + \rho_{\text{block}}(T_{\text{block,avg}})\end{aligned}\quad (1)$$

where the input variables are input reactivity  $\rho_{\text{in}}(t)$ , average fuel temperature  $T_{\text{fuel,avg}}$ , and average moderator temperature  $T_{\text{block,avg}}$ . The output variable is the fission power  $P_{\text{fiss}}(t)$ . Known parameters include the fractions of six groups of delayed neutrons  $\beta_{i=1\dots6}$ , the mean neutron generation time  $\Lambda$ , and the decay constants  $\lambda_{i=1\dots6}$ . The intermediate variable is the concentration of delayed neutron precursors  $C_{i=1\dots6}(t)$ .

The initial conditions for the differential equations are

$$\begin{aligned}\frac{dP_{\text{fiss}}(t=0)}{dt} &= 0 \\ \frac{dC_i(t=0)}{dt} &= 0 \quad i = 1, 2, \dots, 6 \\ P_{\text{fiss}}(t=0) &= P_{\text{fiss},0}\end{aligned}\quad (2)$$

where  $P_{\text{fiss},0}$  is the initial fission power.

The temperature feedback coefficients of the fuel and moderator, as well as the neutron kinetics parameters, are based on the pin-block reactor configuration from the Prometheus project [27] and are calculated using the Monte Carlo code RMC[28].

Geometrically, the horizontal and vertical cross-sections of the reactor core are shown in Figure 11. A large safety rod is positioned at the center of the core.

Regarding material settings, the core uses 90% enriched UO<sub>2</sub> fuel, beryllium as the radial movable reflector, and Mo-47.5%Re alloy as the structural support and spectrum shift absorber.

For Monte Carlo calculations, 100,000 neutron simulations are set, with 300 iterations per generation, ignoring the results of the first 30 generations.

In the case settings, the impact of Doppler effect and thermal expansion due to temperature changes on reactivity is considered. Specifically, this includes changes in material density and geometric dimensions due to temperature, changes in absorption and fission cross-sections, and the effect of temperature on scattering cross-sections. Therefore, at each temperature point, not only are the temperature data for each nuclide

considered, but geometry and material density are also reset according to the uniform expansion hypothesis to reflect macroscopic thermal expansion and contraction effects.

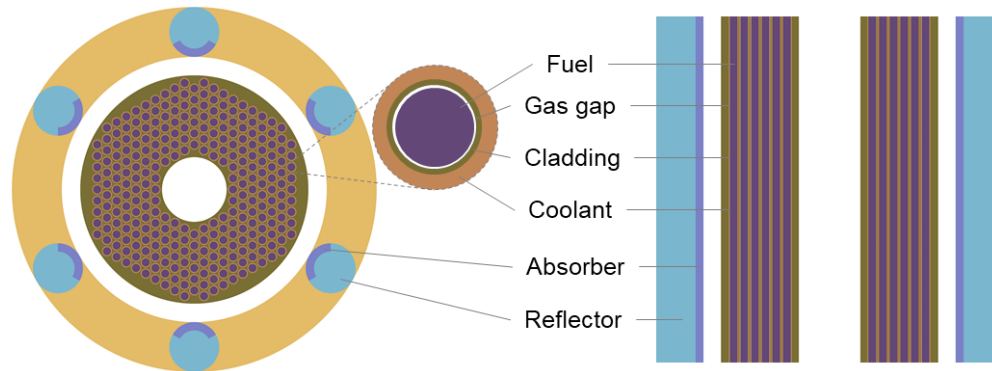


Figure 11 Horizontal and vertical cross-section of the reactor core

The temperature reactivity relationship of the fuel is fitted with a third-order polynomial, as shown in Figure 12 (a). The maximum absolute reactivity deviation of the fit is  $9.54 \times 10^{-4}$ . The temperature reactivity relationship of the moderator is fitted with a third-order polynomial, as shown in Figure 12 (b). The maximum absolute reactivity deviation of the fit is  $1.49 \times 10^{-4}$ .

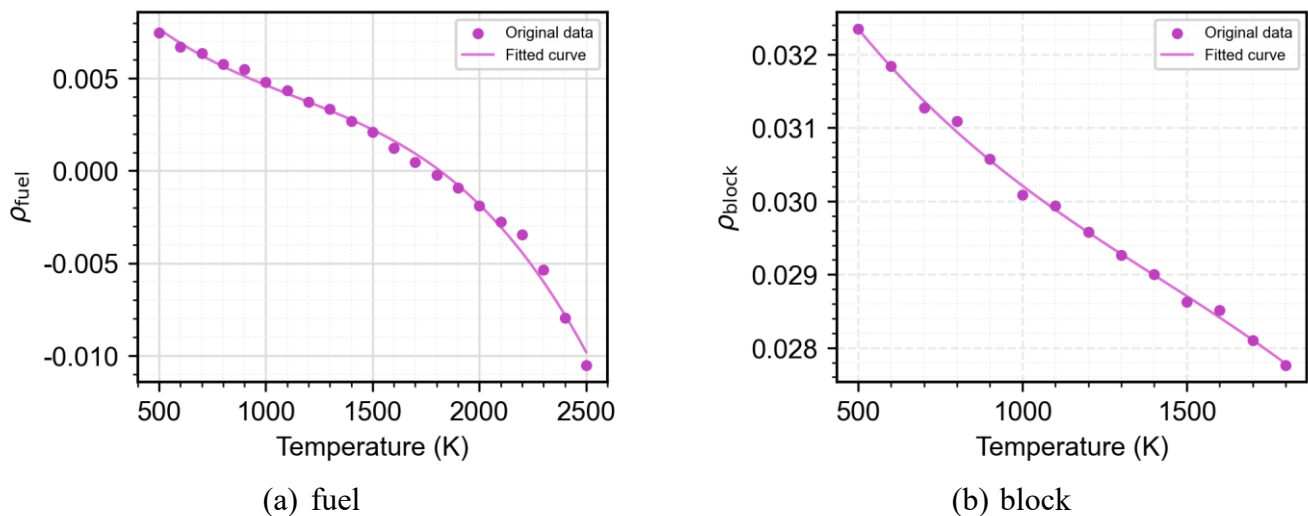


Figure 12 Temperature reactivity of the fuel and the block

### 2.2.2.2 Core thermal-hydraulics

According to Figure 11, the basic structural units of the core from inside to outside are fuel, gap and cladding, coolant channels, and block. At the same radial position, these units are approximately uniformly arranged in a hexagonal pattern. Thus, each ring of hexagonal units can be considered as a single channel with a uniformly distributed radial arrangement in the polar coordinate system. Multiple such single

channels together form the core, with energy transfer between channels occurring through the thermal conductivity of the block. Therefore, the core can be viewed as a multi-channel structure.

This multi-channel core structure is based on the following assumptions: (1) The materials in each part of a single channel are homogeneous; (2) Heat conduction occurs only within the fuel, cladding, gap, and moderator, with no thermal contact resistance at the interfaces; (3) Only convective heat transfer occurs between the block and coolant; (4) No heat conduction occurs within the coolant channel of each single channel, and the physical parameters of the coolant are lumped radially and vary only axially; (5) The cladding and gap have negligible thermal capacity due to their much smaller thickness compared to the fuel and moderator, thus they are assumed to have only thermal resistance. The multi-channel reactor core assumption is shown in Figure 13.

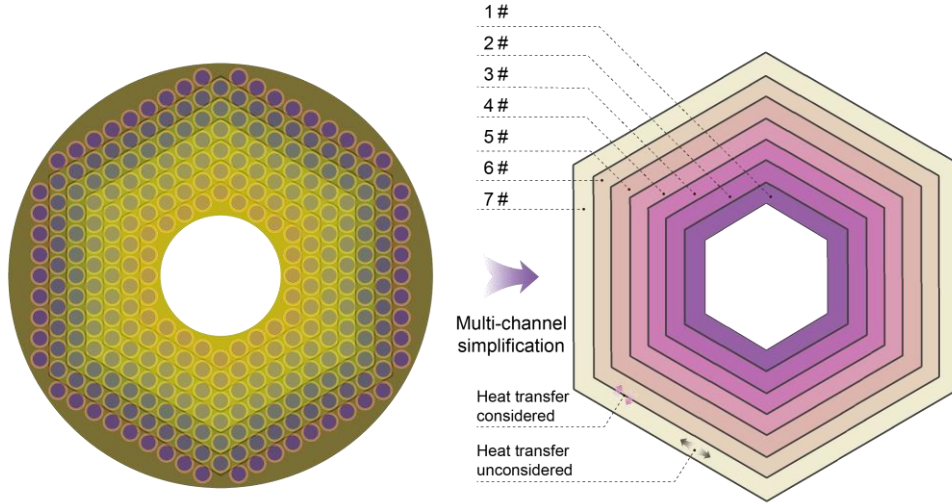


Figure 13 Multi-channel assumption for reactor core

The fuel interior satisfies the following partial differential equation

$$\frac{\partial(\rho_f c_{p,f} T_f)}{\partial t} = \frac{1}{r} \frac{\partial}{\partial r} \left( r k_f \frac{\partial T_f}{\partial r} \right) + k_f \frac{\partial^2 T}{\partial z^2} + Q_f \quad (3)$$

At the boundary in the  $z$  direction, the adiabatic condition is satisfied; at the boundary in the  $r$  direction, it is connected to the adjacent gap region through the same temperature. Here,  $\rho_f$  represents the fuel density in  $\text{kg}/\text{m}^3$ ;  $c_{p,f}$  represents the specific heat capacity of the fuel in  $\text{J}/(\text{kg}\cdot\text{K})$ ;  $T_f$  represents the fuel temperature in  $\text{K}$ ;  $t$  represents time in  $\text{s}$ ;  $r$  represents the radial coordinate in  $\text{m}$ ;  $k_f$  represents the thermal conductivity of the fuel in  $\text{W}/(\text{m}\cdot\text{K})$ ;  $z$  represents the axial coordinate in  $\text{m}$ ;  $Q_f$  represents the heat source term within the fuel, calculated from the output  $P_{\text{fiss}}$  of the neutron kinetics model and the total volume of the core fuel in  $\text{W}/\text{m}^3$ .

The mass conservation equation states that the sum of the change in gas density over time and the change in mass flow rate over space at a given cross-section in the pipeline is zero, expressed as

$$\frac{\partial \rho_g}{\partial t} + \frac{\partial}{\partial z} \left( \frac{\dot{m}}{A_p} \right) = 0 \quad (4)$$

where,  $\rho_g$  represents the gas density in kg/m<sup>3</sup>;  $\dot{m}$  represents the gas mass flow rate in kg/s;  $A_p$  represents the flow channel cross-sectional area in m<sup>2</sup>.

The momentum conservation equation is expressed as

$$\frac{\partial}{\partial t} \left( \frac{\dot{m}}{A_p} \right) + \frac{\partial}{\partial z} \left( \frac{\dot{m}^2}{\rho_g A_p^2} \right) = -\frac{\partial p_p}{\partial z} - \frac{f_p \dot{m} |\dot{m}|}{2D_p \rho_g A_p^2} - \rho_g g \cos(\theta) \quad (5)$$

where on the left side, the first term represents the change in momentum over time, and the second term represents the change in momentum over space. On the right side, the first term is the momentum change due to the pressure gradient, the second term is the momentum loss due to wall friction, and the third term represents the gravity term (which is small in deep space). Here,  $p_p$  represents the gas pressure in Pa;  $f_p$  represents the Darcy friction factor (dimensionless);  $D_p$  represents the hydraulic diameter of the pipe in meters;  $\theta$  represents the angle between the gas flow direction and the positive z-axis in radians. The expression for the Darcy friction factor can be found in reference [29], and is expressed as

$$f = \begin{cases} \frac{64}{Re}, Re < Re_L \\ f_L + \frac{f_T - f_L}{Re_T - Re_L} (Re - Re_L), Re_L < Re < Re_T \\ \left( -1.8 \lg \left( \left( \frac{\varepsilon}{3.7 D_h} \right)^{1.11} + \frac{6.9}{Re} \right) \right), Re > Re_T \end{cases} \quad (6)$$

The energy conservation equation is expressed as

$$\frac{\partial (\rho_g c_p T)}{\partial t} + \frac{\partial}{\partial z} \left( \frac{\dot{m} c_p T}{A_p} \right) = Q_{in} + Q_{out} \quad (7)$$

where on the left side, the first term represents the change in the internal energy of the gas over time, and the second term represents the change in energy over space. On the right side, the two terms represent the heat transferred to the gas from the inner wall and the outer wall, respectively. Here,  $c_p$  represents the specific heat capacity of the

gas in J/(kg·K);  $T$  represents the gas temperature in K;  $Q_{in}$  represents the heat transfer from the inner wall in W;  $Q_{out}$  represents the heat transfer from the outer wall in W.

The geometric characteristics of the flow channel are expressed as

$$A_p = \pi(r_{out}^2 - r_{in}^2), L = 2\pi(r_{in} + r_{out}), D_p = \frac{4A_p}{L} \quad (8)$$

where  $r_{in}$  represents the inner radius of the pipe in meters;  $r_{out}$  represents the outer radius of the pipe in meters;  $L$  represents the perimeter of the pipe in meters.

The heat transfer equation between the coolant and the channel wall is expressed as

$$Q_{in} = \frac{h_{in} \cdot 2\pi r_{in} (T_{in} - T_g)}{A_p}$$

$$Q_{out} = \frac{h_{out} \cdot 2\pi r_{out} (T_{out} - T_g)}{A_p} \quad (9)$$

where  $h_{in}$  represents the inner heat transfer coefficient in W/(m<sup>2</sup>·K);  $h_{out}$  represents the outer heat transfer coefficient in W/(m<sup>2</sup>·K);  $T_{in}$  represents the inner wall temperature in K;  $T_{out}$  represents the outer wall temperature in K;  $T_g$  represents the gas temperature in K.

To obtain the heat transfer coefficients, the Nusselt number is calculated using the relations from references [7,30] as follows

$$Nu_{in} = \frac{(\xi/8)RePr}{1.07 + 12.7\sqrt{(\xi/8)}\left(\frac{2/3}{Pr-1}\right)} \theta_{in}^{-0.5051g\theta_{in}-0.165}$$

$$Nu_{out} = \frac{(\xi/8)RePr}{1.07 + 12.7\sqrt{(\xi/8)}\left(\frac{2/3}{Pr-1}\right)} \theta_{out}^{-0.5051g\theta_{out}-0.165} \quad (10)$$

$$Re = \frac{\dot{m}_p D_p}{A_p \mu}, \xi = (1.82 \log Re - 1.64)^{-2}$$

$$\theta_{in} = T_{in} / T_g, \theta_{out} = T_{out} / T_g, h_{in} = \frac{Nu_{in} \lambda}{D_p}, h_{out} = \frac{Nu_{out} \lambda}{D_p}$$

where  $Nu_{in}$  represents the inner Nusselt number;  $Nu_{out}$  represents the outer Nusselt number;  $\theta_{in}$  represents the inner temperature ratio;  $\theta_{out}$  represents the outer temperature ratio;  $\lambda$  represents the thermal conductivity in W/(m·K);  $\xi$  represents the friction factor; Re represents the Reynolds number; and  $\mu$  represents the dynamic viscosity of the gas in Pa·s.

Finally, these physical properties are calculated using the non-ideal gas property model for helium-xenon mixtures, expressed as

$$\mu = \mu(T, p), \lambda = \lambda(T, p), c_p = c_p(T, p), Pr = Pr(T, p), \rho = \rho(T, p) \quad (11)$$

### 2.2.3 Turbomachinery

This paper uses the Capstone C-30[31] compressor and turbine model. This model calculates the pressure and temperature changes through the compressor and turbine based on characteristic curves. The characteristic curves express the relationship between the pressure ratio, temperature ratio, dimensionless flow rate, and dimensionless rotational speed.

First, let's explain these four physical quantities. The pressure ratio,  $p_{o2} / p_{o1}$  or  $p_{o4} / p_{o5}$ , represents the ratio of higher total pressure to lower total pressure. The temperature ratio,  $T_{o2} / T_{o1}$  or  $T_{o4} / T_{o5}$ , represents the ratio of higher total temperature to lower total temperature. Subscripts 1, 2, 4, and 5 correspond to the compressor inlet, compressor outlet, turbine inlet, and turbine outlet, respectively. The subscript "o" in the characteristic curves indicates total pressure or total temperature.

The dimensionless flow rate  $\dot{m}'$  and dimensionless rotational speed  $N'$  are the actual flow rate and rotational speed corrected to dimensionless quantities, used to standardize performance comparisons under different operating conditions. The calculation formulas are as follows

$$\dot{m}' = \frac{\dot{m} \cdot \sqrt{\frac{T_{in} R_o}{\gamma}}}{(2r_{tip})^2 P_{in}} \quad (12)$$

$$N' = \frac{N \cdot 2r_{tip}}{\sqrt{\gamma R_o T_{in}}}$$

where  $\dot{m}$  is the actual mass flow rate in kg/s;  $T_{in}$  is the inlet total temperature in K;  $P_{in}$  is the inlet total pressure in Pa;  $R_o$  is the gas constant in J/(kg·K);  $\gamma$  is the specific heat ratio equal to 1.67;  $r_{tip}$  is the impeller outer diameter, 0.05081 m for the compressor and 0.05461 m for the turbine;  $N$  is the actual rotational speed in rpm. Additionally, the design rotational speed for the compressor is 1605 rev/s and for the turbine is 1600 rev/s.

Secondly, the relationships that these four physical quantities satisfy are as follows



$$\frac{P_{o2}}{P_{o1}} = f_{prC}(\dot{m}', N'), \frac{P_{o4}}{P_{o5}} = f_{prT}(\dot{m}', N') \quad (13)$$

$$\frac{T_{o2}}{T_{o1}} = f_{TrC}(\dot{m}', N'), \frac{T_{o4}}{T_{o5}} = f_{TrT}(\dot{m}', N')$$

where  $f_{prC}$  represents the compressor pressure ratio function;  $f_{prT}$  represents the turbine pressure ratio function;  $f_{TrC}$  represents the compressor temperature ratio function;  $f_{TrT}$  represents the turbine temperature ratio function. These functions are obtained by polynomial fitting as described in reference[31], and the compressor pressure ratio and temperature ratio curves can be seen in Figure 14 and Figure 15, respectively. The dashed line on the left represents the compressor surge boundary.

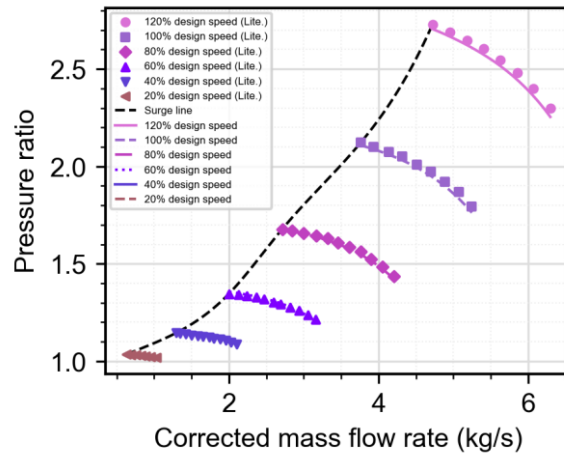


Figure 14 Compressor pressure ratio curve

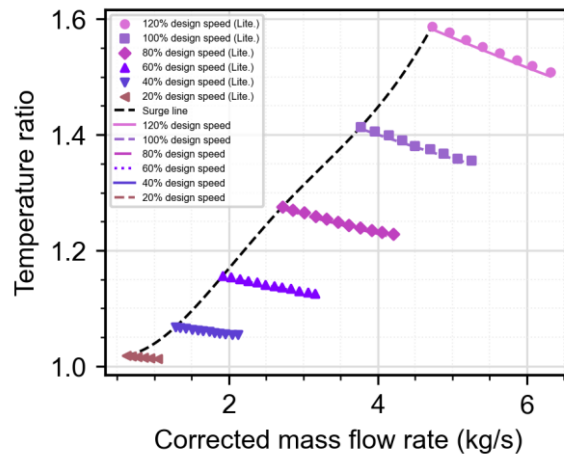


Figure 15 Compressor temperature ratio curve

The turbine pressure ratio and temperature ratio curves are shown in Figure 16 and Figure 17, respectively.

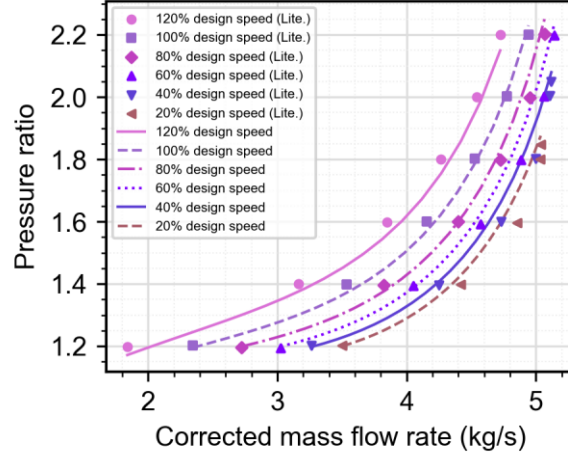


Figure 16 Turbine pressure ratio curve

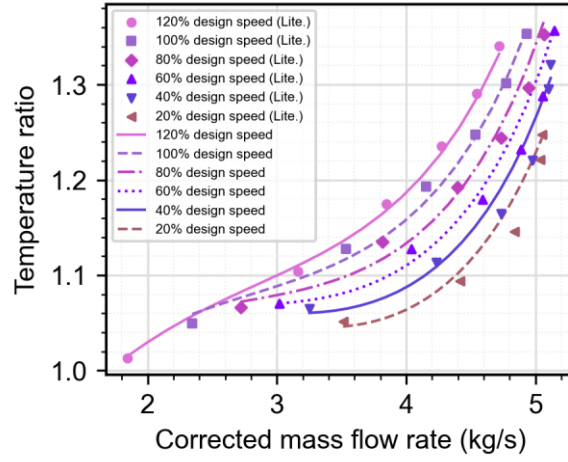


Figure 17 Turbine temperature ratio curve

In dynamic analysis, the power balance among the coaxial compressor, turbine, and generator in the Brayton system is expressed as

$$\begin{aligned}
 P_{\text{shaft}} &= P_T - P_C - P_{\text{alt}} \\
 P_T &= W \cdot (c_{p,T,\text{in}} T_{T,\text{in}} - c_{p,T,\text{out}} T_{T,\text{out}}) \\
 P_C &= W \cdot (c_{p,C,\text{out}} T_{C,\text{out}} - c_{p,C,\text{in}} T_{C,\text{in}}) \\
 P_{\text{shaft}} &= I \cdot \omega_{\text{shaft}} \frac{d\omega_{\text{shaft}}}{dt}
 \end{aligned} \tag{14}$$

where  $P_{\text{shaft}}$  is the net shaft power;  $P_T$  is the turbine power output;  $P_C$  is the compressor power consumption;  $P_{\text{alt}}$  is the alternator power output;  $W$  is the mass flow rate;  $c_{p,T,\text{in}}$  and  $c_{p,T,\text{out}}$  are the specific heat capacities at the turbine inlet and outlet, respectively;  $T_{T,\text{in}}$  and  $T_{T,\text{out}}$  are the temperatures at the turbine inlet and outlet, respectively;  $c_{p,C,\text{in}}$  and  $c_{p,C,\text{out}}$  are the specific heat capacities at the compressor inlet and outlet, respectively;  $T_{C,\text{in}}$  and  $T_{C,\text{out}}$  are the temperatures at the compressor inlet and outlet,

respectively;  $I$  is the moment of inertia of the shaft; and  $\omega_{\text{shaft}}$  is the angular velocity of the shaft.

## 2.2.4 Recuperator

The recuperator uses two counterflow helium-xenon gas channels connected through conductive components. In terms of control equations, the helium-xenon gas flow and heat transfer equations are the same as those within the core, and the conductive components follow a heat conduction control equation similar to that of the fuel, but without a heat source term. For boundary conditions, the outer surfaces of the two channels have adiabatic boundary conditions, and the flow boundaries are connected to adjacent components through pressure, temperature, and mass flow rate.

## 2.2.5 Cooler

The cooler is a helium-xenon flow channel similar to those in the core, with a simplified radiation boundary condition on the pipe wall, adjusted for heat dissipation area. The control equation is

$$h_{\text{out}}(T_{\text{out}} - T_{\text{g}}) = -\frac{S_{\text{ts}}}{S_{\text{rs}}} \varepsilon \sigma (T_{\text{out}}^4 - T_{\text{space}}^4) \quad (15)$$

where  $\varepsilon$  is the emissivity of the cooler;  $T_{\text{out}}$  is the wall temperature on the outside of the pipe;  $T_{\text{space}}$  is the space temperature;  $S_{\text{ts}}$  is the surface area of the cooler's pipe wall;  $S_{\text{rs}}$  is the effective heat dissipation area of the cooler.

# 3 Verification of models

## 3.1 Steady-state verification

This paper uses a reactor connected to a single Brayton system. Reference[31] from the Prometheus project's JIMO initiative describes a system with one reactor and two Brayton systems (dual-loop), but for simulation, it used one reactor and one Brayton system (single-loop). For comparison with previous work, this paper also uses the single-loop configuration.

To verify the correctness of the system program, this paper compares the results obtained after the system runs transiently to steady state at rated power. The thermal line calculation results for the single-loop Brayton reactor system are from the literature,

with temperature, pressure, and flow rate at various points obtained from Sandia National Laboratories' design codes FEPSIM and RxPwrSys[31]. The comparison of this paper's results with those in the literature can be seen in Table 1. Parameter deviations are within 10%, with pressure-related parameters mostly around 7% and temperature-related parameters ranging from -0.8% to -9.6%. The differences may be due to:

1. Differences in core simplification assumptions. The literature uses a single average fuel rod with only axial distribution, while this paper uses a multi-channel core model with both axial and radial distributions.

2. Differences in physical property parameters. The literature assumes constant specific heat capacity for the helium-xenon mixture, while this paper updates gas properties in real-time according to the virial equation and dense gas correction theory with changing temperature and pressure.

3. Differences in component pressure drop assumptions. The literature does not consider the pressure drop in the recuperator and cooler, while this paper details the pressure drops due to friction in each component.

Given the system's complexity and that most parameter deviations are within acceptable ranges, these verification results can be considered acceptable. Although the maximum deviation is slightly higher, it remains reasonable for such a complex system.

Table 1 Comparison of steady-state thermal line results at rated conditions

	Reference[31,41]	Calculated	Relative error (%)
Compressor inlet temperature (K)	319.0	304.8	-4.5
Compressor outlet temperature (K)	470.0	427.4	-9.1
Compressor inlet pressure (MPa)	1.50	1.50	0.0
Compressor outlet pressure (MPa)	3.00	2.79	-7.0
Turbine inlet temperature (K)	1147.0	1111.7	-3.1
Turbine outlet temperature (K)	908.0	887.8	-2.2
Turbine inlet pressure (MPa)	2.97	2.74	-7.7
Turbine outlet pressure (MPa)	1.50	1.51	0.7
Cooler inlet temperature (K)	463.0	418.5	-9.6
Turbine inlet pressure (MPa)	1.50	1.50	0.0
Core inlet temperature (K)	885.0	877.6	-0.8
Core inlet pressure (MPa)	3.00	2.78	-7.3
Mass flow rate (kg/s)	3.10	3.31	6.8

### 3.2 Transient verification

This paper follows the startup method from reference[31], dividing the startup process into five stages. The control variables are core reactivity insertion, turbine alternator system shaft speed, and cooler outer side radiation sink temperature. The variations of these variables over time are shown in Figure 18.

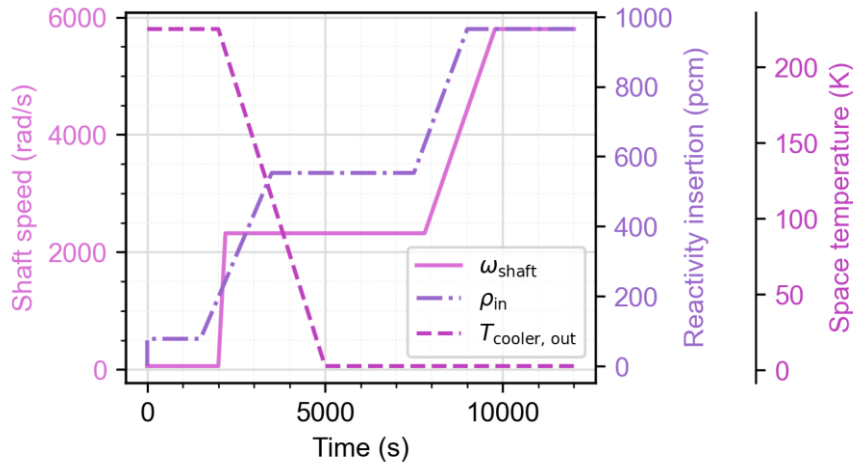


Figure 18 Control variables during the startup process

Stage 1 (0-1500 seconds): Zero power startup. Initially, the core power is only a few watts. A constant reactivity of 78 pcm is introduced and maintained for 1500 seconds, until the fission power reaches approximately 1.6 kW and the average core temperature reaches 292 K.

Stage 2 (1500-3500 seconds): Reactivity ramp insertion. During this period, reactivity increases at a constant rate, reaching 553 pcm by 3500 seconds. Around 2000 seconds, when the average core temperature reaches approximately 400 K, the turbine alternator system starts. Over the next 200 seconds, the shaft speed rises to 40% of the rated speed, initiating the Brayton system. As shown in Figure 19, the flow rate increases rapidly. At the moment of shaft speed initiation, the radiation sink temperature on the cooler's outer side begins to drop, reflecting the deployment of the cooling panels, providing a cold source for the Brayton system post-startup. Due to increased cooling power, the compressor inlet and outlet temperatures decrease to some extent, as seen in Figure 21.

Stage 3 (3500-7500 seconds): Low power steady state. During this period, reactivity and shaft speed remain stable, and the cooler outer side temperature continues to decrease, reaching the cosmic background radiation temperature of 2.725 K by 5000 seconds. Around 6000 seconds, the system reaches a steady state. By the end of this

stage, the average fuel temperature is 618 K, fission power is 45 kWt, core inlet and outlet enthalpy rise is 43 kWt, and generator output power is 10 kWe.

Stage 4 (7500-9780 seconds): Transition to full power. Starting at 7500 seconds, reactivity increases at a constant rate by 412 pcm, ending at 9000 seconds. Shaft speed begins to ramp up at 7800 seconds, reaching 100% rated speed by 9780 seconds. Reactor power increases approximately linearly, as shown in Figure 20.

Stage 5 (after 9780 seconds): Full power steady state. Around 10,000 seconds, the Brayton system reaches full power steady state. At this point, the average fuel temperature is 1056 K, core outlet temperature is 1066 K, and core outlet pressure is 2.72 MPa. The core fission power is 416 kWt, the core inlet and outlet enthalpy rise is 390 kWt, and the generator output power is 98 kWe, with an efficiency of 25.13%.

The comparison of core power during the startup process with that in reference[31] is shown in Figure 20. It can be seen that the core power trends are similar, but there are some differences during the second stage of reactivity ramp insertion and the final full power steady state. In this work, the first power increase of the core occurs earlier compared to the reference, due to the higher initial power of the core at the beginning of the startup, leading to greater power changes during the period of constant reactivity insertion. At the final full power steady state, the higher total reactivity insertion in this work results in a higher steady state power, with the core outlet temperature closer to the Brayton system loop's design value of 1144 K.

The comparison of turbine inlet temperature with the data from literature[31] is shown in Figure 21. It can be observed that, in the second phase, the temperature increase rate is slower and the peak temperature is lower than the literature data. This is because the time taken for the shaft speed to rise from 0 to 40% was 200 seconds in this study, compared to 100 seconds in the literature. The purpose of this longer duration was to reduce the stiffness of the numerical equations and improve the solving speed. Consequently, more heat accumulated in the core before the shaft speed increased rapidly in the literature, leading to a faster and higher temperature rise at the core outlet, which is the turbine inlet, after the rapid shaft speed startup.

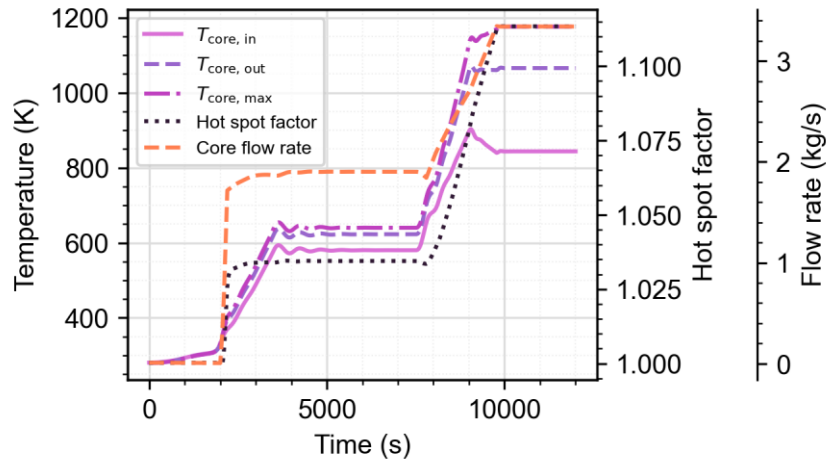


Figure 19 Changes in core temperature indicators and flow rate during the startup

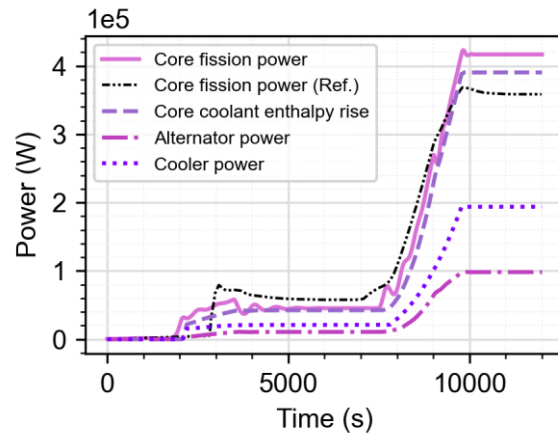


Figure 20 Power changes in various parts of the Brayton system

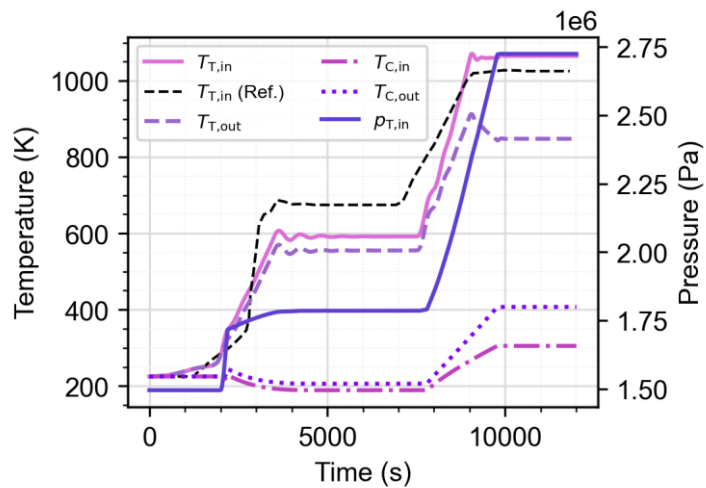


Figure 21 Temperature changes at various points in the Brayton system and turbine inlet pressure changes

## 4 Results and discussion

### 4.1 Reactivity insertion analysis

Performing reactivity insertion accident calculations is essential to understand the system's dynamic behavior and provides insight into the impact of reactivity control on the system's thermodynamics and neutron physics. This section analyzes the effect of inserted reactivity on reactor power, temperature reactivity feedback, peak reactor temperature, and hotspot factor over time.

#### 4.1.1 Power

First, the changes in total power after introducing different step reactivities are shown in Figure 22. After reactivity insertion, there is a significant initial power surge or drop. Subsequently, due to reactivity feedback, the power begins to oscillate. Over time, the power reaches a new equilibrium position, which is positively correlated with the magnitude of the step reactivity introduced. Introducing a larger positive reactivity leads to a higher final power level, but during the feedback oscillations, the power may temporarily drop below the initial equilibrium.

Additionally, the magnitude and timing of the peak power vary with reactivity, as shown in Figure 23. The logarithm of peak power is approximately linear with reactivity, while the peak power timing follows an approximate exponential function. The exponential function is expressed as

$$t_{\text{peak}} = a \cdot e^{b \cdot \rho_{\text{in}}} + c \quad (16)$$

where  $t_{\text{peak}}$  is the peak power time in seconds;  $\rho_{\text{in}}$  is the introduced step reactivity in dollars, with 1 dollar equal to 0.0066817; and  $a, b, c$  are fitting parameters. Using the least squares method, the fitting results show quality of  $R^2 = 0.9997$ . Therefore, the exponential function can describe the timing of the peak power occurrence.



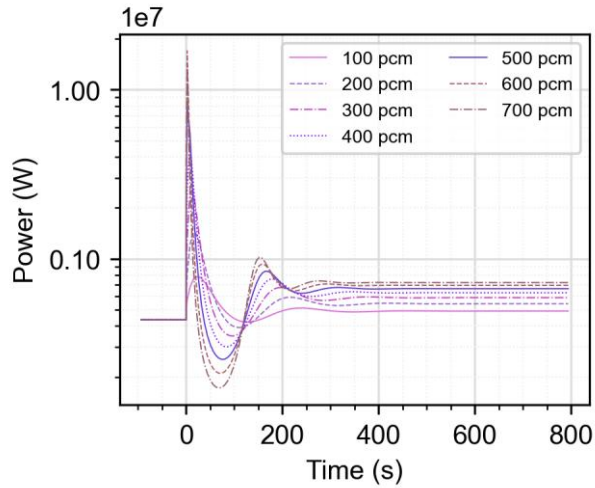


Figure 22 Total power change due to step reactivity insertion

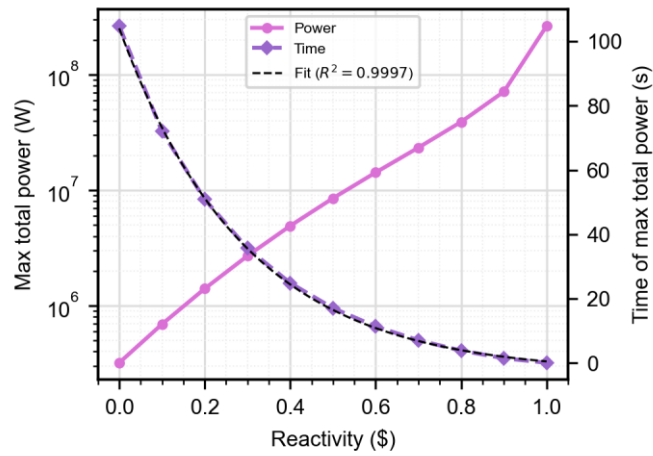


Figure 23 Variation of peak power magnitude and timing with reactivity

#### 4.1.2 Reactivity feedback

After introducing 100 pcm reactivity, changes in various reactivity effects are shown in Figure 24. Fuel expansion and Doppler effect provide about 20 pcm more negative reactivity than the block.

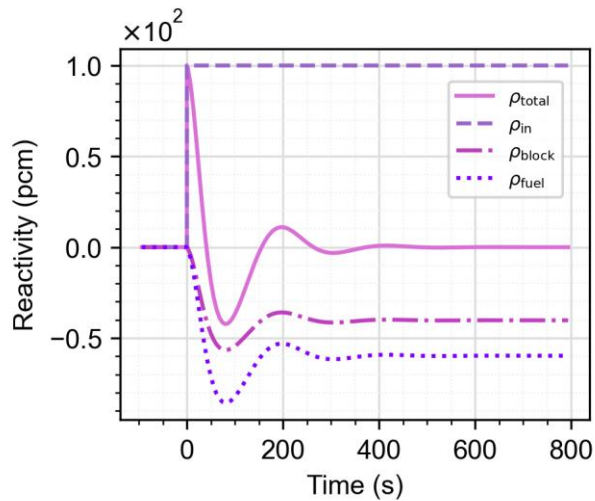


Figure 24 Reactivity effect changes with 100 pcm reactivity insertion

### 4.1.3 Temperature

Reactor core maximum temperature over time is shown in Figure 25. With different positive reactivity insertions, the temperature rapidly rises to a peak, then decreases due to negative feedback, and finally stabilizes at a new level.

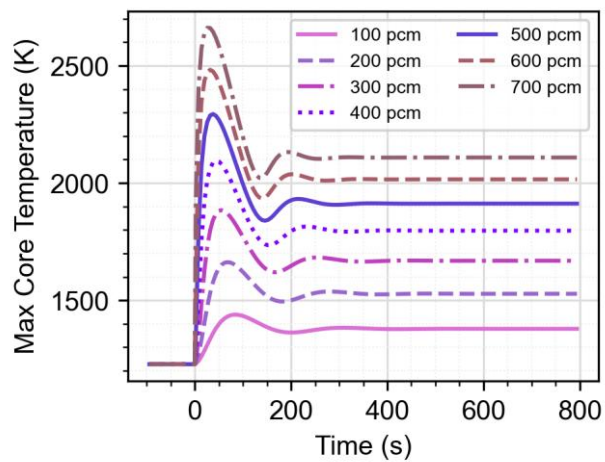


Figure 25 Max temperature over time with different positive step reactivities

The magnitude and timing of the temperature peak vary with reactivity, as shown in Figure 26. The peak temperature increases approximately linearly with reactivity.

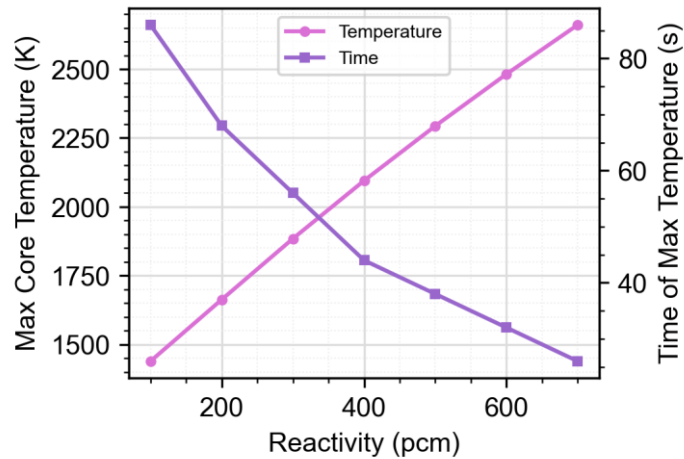


Figure 26 Variation of peak temperature magnitude and timing with reactivity

#### 4.1.4 Hotspot factor

The hotspot factor of the core reflects the power non-uniformity in a multi-channel core. A higher value indicates a larger temperature difference between inner and outer channels. The trend of hotspot factor over time with different reactivity insertions is shown in Figure 27. Shortly after reactivity insertion, the total core power changes significantly, causing a uniform increase in heat generation across the core. The initially cooler regions (typically the outer radial channels) experience more noticeable temperature changes, leading to a rapid decrease in the hotspot factor, even though the overall core temperature is rising, as shown in Figure 28. Subsequently, due to the combined effects of reactivity feedback leading to power reduction and heat transfer, the core's temperature distribution stabilizes at a new steady state, where the hotspot factor is higher than the initial state.

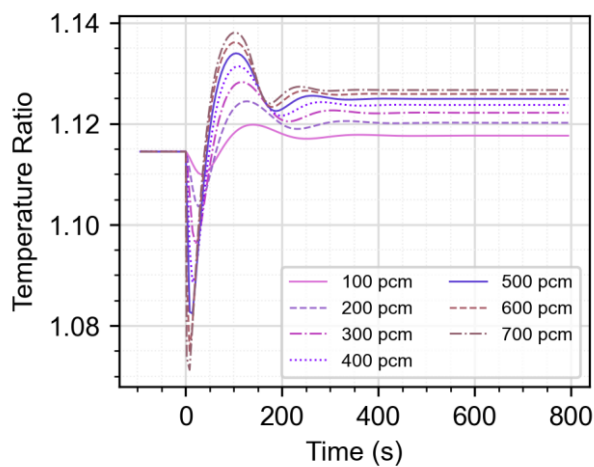


Figure 27 Variation of core hotspot factor with different reactivity insertions

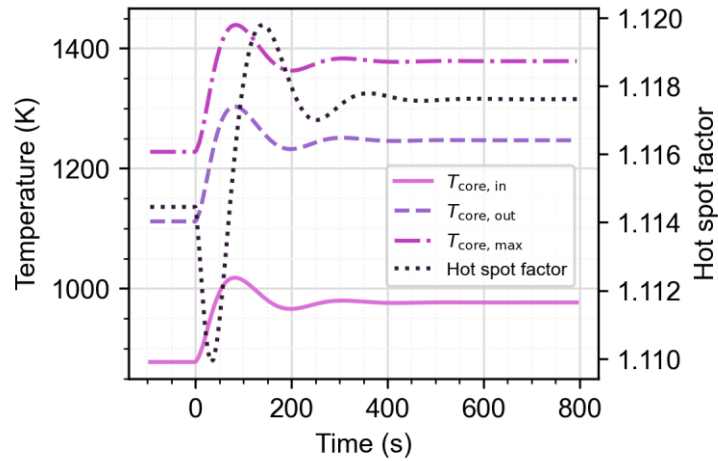


Figure 28 Comparison of core temperature and hotspot factor variations

The ratio of the hotspot factor before and after stabilization varies with reactivity, as shown in Figure 29. Higher reactivity insertion leads to greater overall power changes, causing more drastic temperature variations and further increasing temperature distribution non-uniformity.

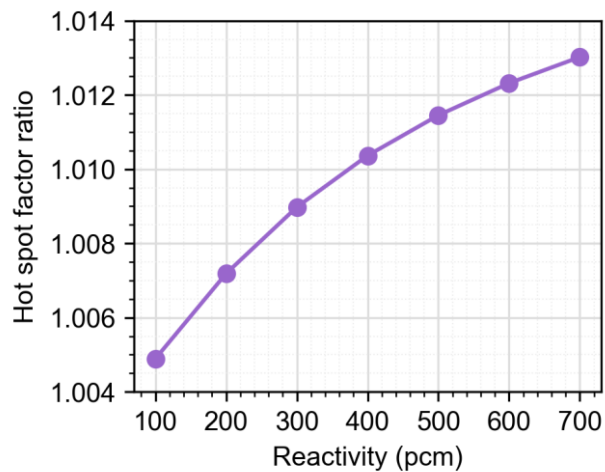


Figure 29 Variation of hotspot factor with reactivity before and after stabilization

## 4.2 Optimization of the startup control

After understanding the overall characteristics of the system, this chapter introduces a method for parameterizing control sequences and an optimization framework to enable the reactor to transition more rapidly from cold start to rated conditions.

### 4.2.1 Problem definition

During the startup process, the low-power steady-state phase lasts too long, and

the reactivity ramp control is not precise, resulting in low overall startup efficiency. To address this issue, this paper employs a multi-objective optimization algorithm to optimize the control sequences of variables such as reactivity insertion, TAC system shaft speed, and cooling system background temperature. The goal is to accelerate the system's achievement of rated power and improve startup efficiency. The optimization involves parameterizing the control sequences, setting performance evaluation metrics, and establishing the algorithmic workflow.

First, the method for parameterizing the control sequences is illustrated in Figure 30. For the shaft speed control sequence, the parameterized control points are 1# through 4#. Point 1# marks the shaft speed start time  $t_1$ , with the parameter being the startup time. Point 2# marks the end of the first increase in shaft speed  $\omega_2$ , with the parameter being the shaft speed percentage at this endpoint. The time interval between points 1# and 2# is fixed at 200 seconds to reflect the rapid startup process in a real scenario while ensuring numerical stability. Point 3# marks the start of the second shaft speed increase, with parameters for the start time  $t_3$  and corresponding shaft speed  $\omega_3$ . Point 4# marks the point at which the shaft speed reaches its rated value, with the parameter being the corresponding time  $t_4$ .

For the reactivity insertion control sequence, the parameterized control points are 5# to 8#. Point 5# marks the end of the zero-power startup phase and the beginning of the first reactivity ramp insertion, with parameters for the corresponding time  $t_5$  and constant reactivity  $\rho_5$  during the zero-power startup. Point 6# is the end of the first reactivity ramp insertion, with parameters for time  $t_6$  and reactivity  $\rho_6$ . Point 7# is the start of the second reactivity ramp insertion, with parameters for time  $t_7$  and reactivity  $\rho_7$ . Point 8# marks the end of reactivity insertion during the startup process, with parameters for the corresponding time  $t_8$ .

For the control sequence of the cooler external temperature, the parameterized control points are 9# and 10#. Point 9# is the start of the cooler panel deployment, with the parameter being the corresponding time  $t_9$ . Point 10# is the end of the deployment, with the parameter being the corresponding time  $t_{10}$ .

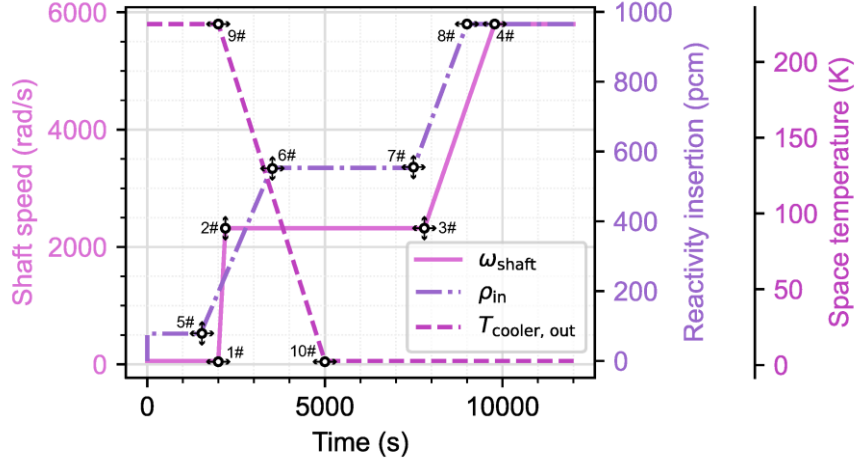


Figure 30 Parameterizing control sequences via movable points

Regarding performance metrics, the focus is on startup efficiency, considering both power and temperature aspects. On one hand, the sooner the fission power first reaches 400 kW, the better. On the other hand, the sooner the core outlet temperature first reaches 1000 K, the better. Therefore, the objective function can be expressed as follows.

$$f_1(\mathbf{x}) = t_{\text{power\_400kW}} \quad (17)$$

$$f_2(\mathbf{x}) = t_{\text{temp\_1000K}} \quad (18)$$

where vector  $\mathbf{x} = (t_1, \omega_2, t_3, \omega_3, t_4, t_5, \rho_5, t_6, \rho_6, t_7, \rho_7, t_8, t_9, t_{10})$  representing control sequence parameters

The primary constraint is time, which must increase sequentially. Therefore, the optimization problem for the control sequence can be described as

$$\begin{aligned} \mathbf{X} &= \arg \min_{\mathbf{x}} (f_1(\mathbf{x}), f_2(\mathbf{x})) \\ \text{subject to } &\begin{cases} t_1 < t_3 < t_4 \\ t_5 < t_6 < t_7 < t_8 \\ t_9 < t_{10} \\ \mathbf{x}_{\min} \leq \mathbf{x} \leq \mathbf{x}_{\max} \end{cases} \end{aligned} \quad (19)$$

#### 4.2.2 Optimization results

The control strategy underwent 20 generations of evolution, with a population size of 100 per generation. Each individual in the population underwent a 10,000-second startup simulation. For successful simulations, the average CPU time was approximately 130 to 150 seconds, resulting in a total CPU time exceeding 75 hours. The optimal values of the two performance metrics per generation during the

optimization process are shown in Figure 31. In the first six generations, all simulations failed due to excessive stiffness of the ordinary differential equations. From the seventh generation onward, the corresponding ODE system could be solved. Significant improvements in both performance metrics were observed after the 10th and 13th generations. The Pareto front of the multi-objective optimization has four dominant solutions, as shown in Figure 32.

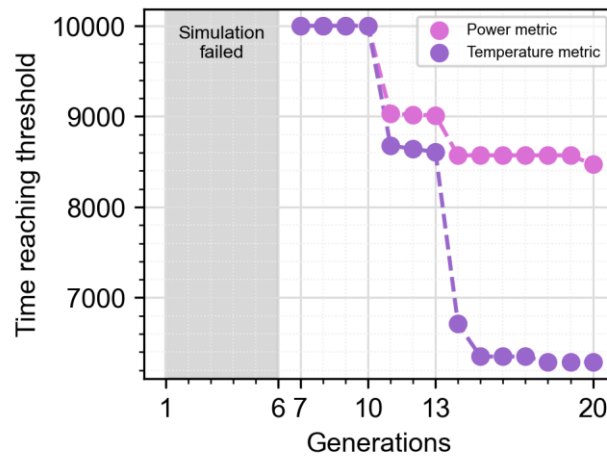


Figure 31 Changes in performance metrics with each generation

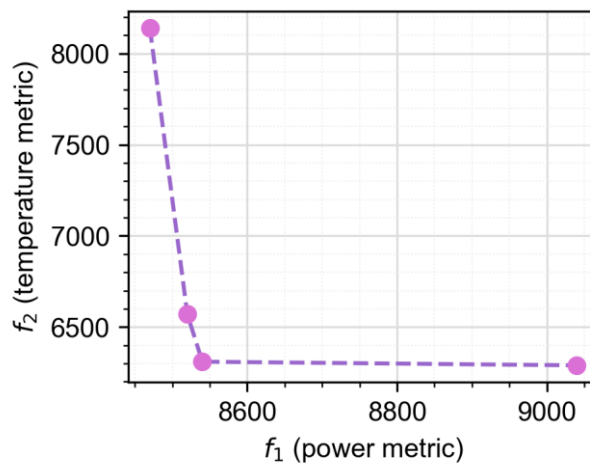


Figure 32 Pareto front of control sequence optimization

The control case, where power and temperature first exceed their thresholds at 8520 seconds and 6570 seconds respectively, was selected for analysis. Compared to the baseline control strategy, the time to reach rated power was reduced by approximately 1260 seconds, and the turbine inlet temperature reached its rated value about 1980 seconds earlier. The time comparisons for each control stage are shown in Table 2 to Table 4. It is evident that the control duration for different variables significantly decreases at different stages. Notably, the duration for reactivity introduction control shows a remarkable reduction, with the time decreasing by 1169.0

seconds from stage 7# to stage 8#, a reduction of 77.9%.

Table 2 Shaft speed control comparison

Phase	Original time (s)	Optimized time (s)	Shortened time (s)	Shortened percentage (%)
Start to 1#	2000.0	1541.6	458.4	22.9
1# to 2#	200.0	200.0	0.0	0.0
2# to 3#	5600.0	4631.0	969.0	17.3
3# to 4#	1980.0	2050.3	-70.3	-3.6

Table 3 Reactivity insertion control comparison

Phase	Original time (s)	Optimized time (s)	Shortened time (s)	Shortened percentage (%)
Start to 5#	1500.0	1128.5	371.5	24.8
5# to 6#	2000.0	1749.8	250.2	12.5
6# to 7#	4000.0	3302.7	697.3	17.4
7# to 8#	1500.0	330.96	1169.0	77.9

Table 4 Cooler temperature control comparison

Phase	Original time (s)	Optimized time (s)	Shortened time (s)	Shortened percentage (%)
Start to 9#	2000.0	1638.8	361.2	18.1
9# to 10 #	3000.0	3294.5	-294.5	-9.8

The control curves for reactivity, shaft speed, and cooler background temperature are shown in Figure 33 to Figure 36, respectively. For reactivity control, the initial cold startup exhibits higher reactivity, transitioning to a low-slope ramp reactivity insertion during the low-power steady state, with a steeper slope at the final ramp insertion. Shaft speed control points occur earlier than before optimization, with the low-power steady state transitioning to a low-slope shaft speed increase. The cooler background temperature control shows minimal difference before and after optimization, indicating it is not a major factor affecting startup process efficiency.



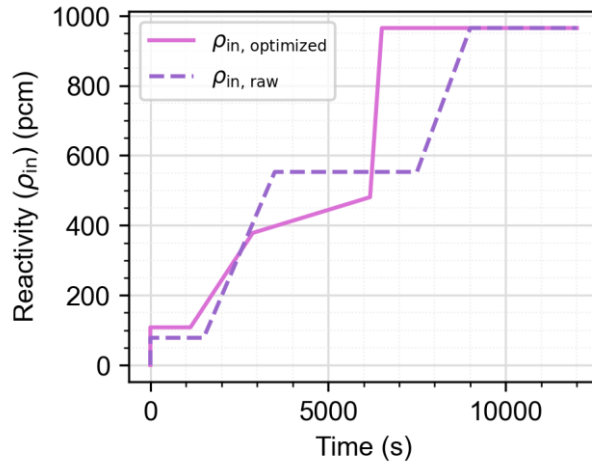


Figure 33 Comparison of reactivity insertion control before and after optimization

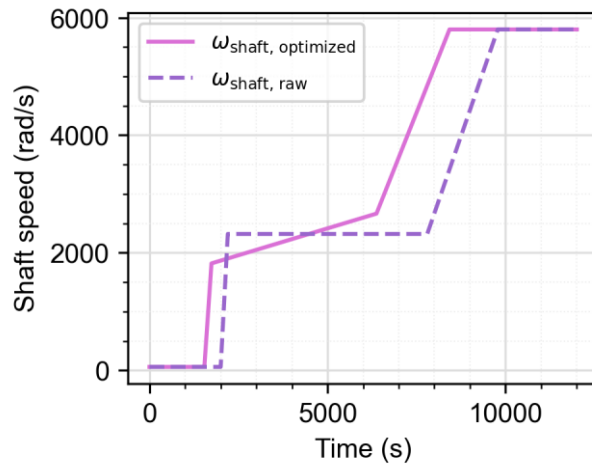


Figure 34 Comparison of shaft speed control before and after optimization

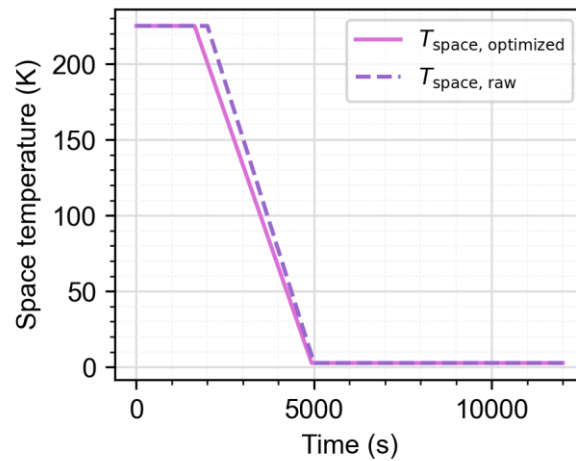


Figure 35 Comparison of cooler temperature control before and after optimization

The effects of the optimized control sequences are reflected in the speed at which power and temperature rise from a cold state to rated conditions. The variation of fission power over time is shown in Figure 36. It can be observed that the reactivity insertion

around 2000 seconds caused larger power fluctuations. Around 6000 seconds, rapid reactivity insertion resulted in a brief, sharp increase in power, but due to negative reactivity feedback, there was a significant power decrease in the following 500 seconds. Subsequently, as the power approached the rated level, the slope of the fission power increase tended to follow the changes in shaft speed.

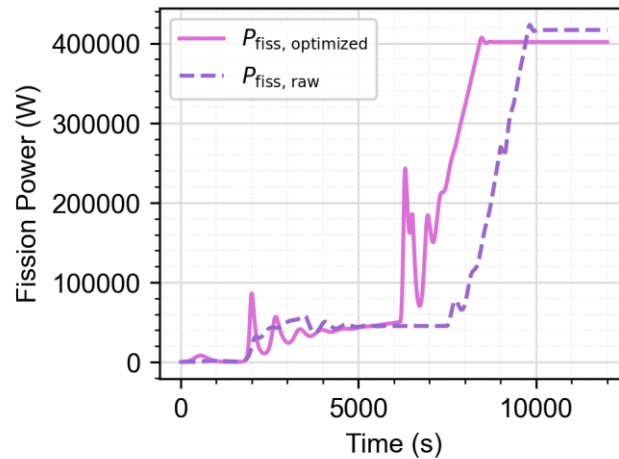


Figure 36 Comparison of fission power control before and after optimization

The turbine inlet temperature is shown in Figure 37. Due to the reduced reactivity at the end of the first reactivity ramp insertion compared to the pre-optimization stage, the temperature is lower around 4000 seconds. Subsequently, around 6000 seconds, the temperature rises rapidly following the swift reactivity insertion, overshoots, and fluctuates before gradually stabilizing to the rated inlet temperature. Overall, the turbine inlet temperature tends to follow the control trend of reactivity.

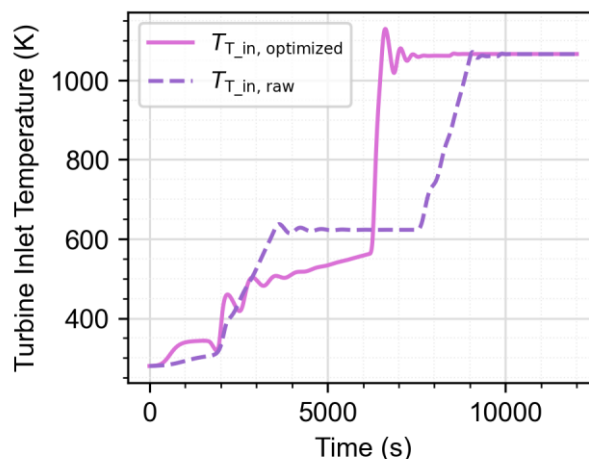


Figure 37 Comparison of turbine inlet temperature control before and after optimization

Additionally, the maximum core temperature, which is critical to the integrity of the core, is illustrated in Figure 38. Overall, the trend is similar to that of the turbine inlet temperature, and the peak temperature remains nearly the same as before

optimization. However, the rapid temperature changes in the core caused by reactivity insertion may result in significant temperature gradients in different regions. This can lead to uneven thermal expansion, potentially causing material cracking, deformation, or structural failure.

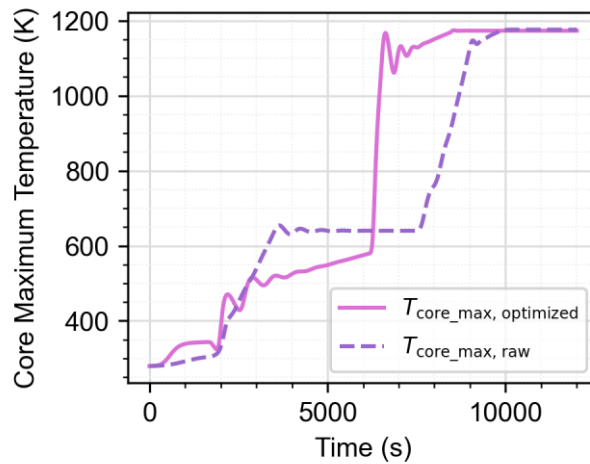


Figure 38 Comparison of core maximum temperature control before and after optimization

## 5 Conclusions

This paper optimized the startup control of He-Xe cooled SNPS through a system analysis program.

Firstly, an analysis toolset was developed for a He-Xe cooled SNPS. The gas property model integrates the virial equation and dense gas correction theory for accurate physical property calculations across various conditions. A multi-channel core model divided the reactor core into multiple channels, using the Monte Carlo code RMC for precise descriptions of temperature reactivity coefficients and neutron kinetics. Steady-state and startup transient verifications confirmed the model's accuracy and reliability, with key parameter deviations mostly within 10%. Quantitative analysis of reactivity insertion accidents revealed that the peak power is logarithmically related to reactivity insertion and the peak temperature is linearly related to reactivity insertion.

Secondly, the startup control was optimized by the proposed control optimization framework, using the system model in the former part. The time to reach rated power was reduced by approximately 1260 seconds, and the turbine inlet temperature reached its rated value about 1980 seconds earlier compared to the baseline control strategy. The optimized control strategy significantly reduced the startup time by adjusting the

reactivity insertion rate, shaft speed, and cooling temperature. For example, the time from 7# to 8# was reduced by 1169.0 seconds, a 77.9% decrease. These adjustments enhanced system startup efficiency, while the acceptable rigidity of the numerical method ensures that physical process changes are slow and smooth.

These findings provide essential technical insights for designing and optimizing nuclear power systems for future deep space missions.

## Declaration of competing interest

The authors declare that they have no known competing financial interests or personal relationships that could have appeared to influence the work reported in this paper.

## Acknowledgements

The authors thank the National Key Laboratory of Nuclear Reactor Technology, Nuclear Power Institute of China for their support.

## CRedit

**Chengyuan Li:** Conceptualization, Methodology, Software, Formal analysis, Investigation, Writing - Original draft preparation. **Jian Deng:** Supervision, Project administration. **Shanfang Huang:** Supervision, Resources, Writing - Review & Editing. **Jiahe Shang:** Data curation, Validation. **Leran Guo:** Data curation, Validation

## Funding sources

This research did not receive any specific grant from funding agencies in the public, commercial, or not-for-profit sectors.

## References

- [1] Araújo, E. F., and Guimarães, L. N. F., 2018, “American Space Nuclear Electric Systems,” *J.Aerosp. Technol. Manag.*, **10**, p. e4418.
- [2] Yan, B. H., Wang, C., and Li, L. G., 2020, “The Technology of Micro Heat Pipe Cooled Reactor: A Review,” *Annals of Nuclear Energy*, **135**, p. 106948.
- [3] Xu, C., Kong, F., Yu, D., Yu, J., and Khan, M. S., 2021, “Influence of Non-Ideal Gas Characteristics on Working Fluid Properties and Thermal Cycle of Space Nuclear Power Generation System,” *Energy*, **222**, p. 119881.
- [4] Ashcroft, J., and Eshelman, C., 2007, “Summary of NR Program Prometheus Efforts,” *AIP Conference Proceedings*, American Institute of Physics, pp. 497–521.
- [5] Wollman, M., and Zika, M., 2006, “Prometheus Project Reactor Module Final Report, For Naval Reactors Information.”
- [6] Dragunov, Y., 2015, “Fast-Neutron Gas-Cooled Reactor for the Megawatt-Class Space Bimodal Nuclear Thermal System,” *Engineering and Automation Problems*, **2**, pp. 117–120.
- [7] Qin, H., Zhang, R., Guo, K., Wang, C., Tian, W., Su, G., and Qiu, S., 2021, “Thermal-Hydraulic Analysis of an Open-Grid Megawatt Gas-Cooled Space Nuclear Reactor Core,” *International Journal of Energy Research*, **45**(8), pp. 11616–11628.
- [8] Koroteev, A., Oshev, Y. A., Popov, S., Karevsky, A., Solodukhin, A. Y., Zakharenkov, L., and Semenkin, A., 2015, “Nuclear Power Propulsion System for Spacecraft,” *Thermal Engineering*, **62**, pp. 971–980.
- [9] Detsis, E., and Worms, J.-C., 2018, “DEMOCRITOS: Demonstrator Projects for MW Class Nuclear Spacecraft,” Berlin, Germany, pp. EPSC2018-1178.
- [10] Jansen, Bauer, and Masson, 2016, “DEMOCRITOS Demonstrators for Realization of Nuclear Electric Propulsion of the European Roadmaps MEGAHIT & DiPoP,” *AEROSPACE TECHNOLOGY JAPAN*, **14**(ists30), pp. 225–233.
- [11] Tinsley, T., Hodgson, Z., Worms, J. C., Detsis, E., Beaurain, A., Lassoudiere, F., Gaia, E., Tosi, M. C., Jansen, F., Bauer, W., Semenkin, A., Masson, F., and Ruault, J. M., 2015, *DEMOCRITOS: Preparing Demonstrators for High Power Nuclear Electric Space Propulsion*, Societe Francaise, France.
- [12] Ruault, J., Masson, F., Worms, J.-C., Detsis, E., Gaia, M. E., Jansen, F., Semenkin, A., and Tinsley, M. T., 2014, “MEGAHIT: Update on the Advanced Propulsion Roadmap for HORIZON2020,” *The 9-Th International PAMIR Conference on Fundamental and Applied MHD, Thermo Acoustic and Space Technologies*, pp. 16–20.
- [13] Jansen, F., Grundmann, J. T., and Maiwald, V., 2019, “High Power Electric Propulsion: MARS plus EUROPA – Already Beyond 2025!,” *36th International Electric Propulsion Conference*, Vienna, Austria, p. A-275.
- [14] Skorlygin, V. V., 2020, “Space Nuclear Power Systems Startup Optimization Methods,” *At Energy*, **128**(2), pp. 65–70.
- [15] Prikot, K. N., and Savin, V. Ya., 1995, “Improved Control Algorithm for TOPAZ-2 System Start-up Conditions,” *AIP Conference Proceedings*, AIP, Albuquerque, New Mexico (USA), pp. 549–554.
- [16] Zeng, W., Jiang, Q., Liu, Y., Yan, S., Zhang, G., Yu, T., and Xie, J., 2021, “Core Power Control of a Space Nuclear Reactor Based on a Nonlinear Model and Fuzzy-PID Controller,” *Prog. Nucl. Energy*, **132**, p. 103564.
- [17] Ma, Y., Zhong, R., Yu, H., Huang, S., Tian, C., He, X., Ouyang, Z., Liu, J., Liu, Y., and Chai, X., 2022, “Startup Analyses of a Megawatt Heat Pipe Cooled Reactor,” *Progress in Nuclear Energy*, **153**, p. 104405.

- [18] Dong, Z., Cheng, Z., Zhu, Y., Huang, X., Dong, Y., and Zhang, Z., 2023, "Review on the Recent Progress in Nuclear Plant Dynamical Modeling and Control," *Energies*, **16**(3), p. 1443.
- [19] McCann, L. D., 2007, "Use of RELAP5-3D for Dynamic Analysis of a Closed-Loop Brayton Cycle Coupled To a Nuclear Reactor," *AIP Conference Proceedings*, AIP, Albuquerque, New Mexico (USA), pp. 541–550.
- [20] El-Genk, M., Tournier, J.-M. P., and Gallo, B. M., 2010, "Dynamic Simulation of a Space Reactor System with Closed Brayton Cycle Loops," *Journal of Propulsion and Power*, **26**, pp. 394–406.
- [21] Wang, C., Zhang, R., Guo, K., Zhang, D., Tian, W., Qiu, S., and Su, G., 2021, "Dynamic Simulation of a Space Gas-Cooled Reactor Power System with a Closed Brayton Cycle," *Front. Energy*, **15**(4), pp. 916–929.
- [22] Geng, X., and Wang, J., 2024, "Simplified Reactor Model for Microreactor Coupled with Helium Closed Brayton Cycle," *Nuclear Technology*, **210**(6), pp. 941–957.
- [23] Ma, W., Ye, P., Gao, Y., and Yang, X., 2022, "Comparative Study on Sequential and Simultaneous Startup Performance of Space Nuclear Power System with Multi Brayton Loops," *Acta Astronautica*, **199**, pp. 142–152.
- [24] Tournier, J.-M., El-Genk, M., and Gallo, B., 2006, "Best Estimates of Binary Gas Mixtures Properties for Closed Brayton Cycle Space Applications," *4th International Energy Conversion Engineering Conference and Exhibit (IECEC)*, American Institute of Aeronautics and Astronautics, San Diego, California.
- [25] Dragunov, Yu. G., Romadova, E. L., Gabaraev, B. A., Belyakov, M. S., and Derbenev, D. S., 2019, "Recommendations on Calculation of Transport Coefficients and Thermodynamic Properties of Helium-Xenon Gas Mixtures," *Nuclear Engineering and Design*, **354**, p. 110196.
- [26] Johnson, P. K., Corporation, A., and Park, B., 2006, "A Method for Calculating Viscosity and Thermal Conductivity of a Helium-Xenon Gas Mixture."
- [27] Levine, B., 2006, *Space Nuclear Power Plant Pre-Conceptual Design Report, for Information*, Knolls Atomic Power Lab.(KAPL), Niskayuna, NY (United States).
- [28] Wang, K., Li, Z., She, D., Xu, Q., Qiu, Y., Yu, J., Sun, J., Fan, X., Yu, G., and others, 2015, "RMC—A Monte Carlo Code for Reactor Core Analysis," *Annals of Nuclear Energy*, **82**, pp. 121–129.
- [29] Haaland, S. E., 1983, "Simple and Explicit Formulas for the Friction Factor in Turbulent Pipe Flow," *Journal of Fluids Engineering*, **105**(1), pp. 89–90.
- [30] Qin, H., Wang, C., Tian, W., Qiu, S., and Su, G., 2022, "Experimental Investigation on Flow and Heat Transfer Characteristics of He-Xe Gas Mixture," *International Journal of Heat and Mass Transfer*, **192**, p. 122942.
- [31] Wright, S. A., Lipinski, R. J., Vernon, M. E., and Sanchez, T., 2006, *Closed Brayton Cycle Power Conversion Systems for Nuclear Reactors*, Sandia National Lab.(SNL-NM), Albuquerque, NM (United States).
- [32] Price, K., Storn, R. M., and Lampinen, J. A., 2006, *Differential Evolution: A Practical Approach to Global Optimization*, Springer Science & Business Media.
- [33] Hansen, N., and Ostermeier, A., 2001, "Completely Derandomized Self-Adaptation in Evolution Strategies," *Evolutionary Computation*, **9**(2), pp. 159–195.
- [34] Runarsson, T. P., and Yao, X., 2005, "Search Biases in Constrained Evolutionary Optimization," *IEEE Transactions on Systems, Man, and Cybernetics, Part C (Applications and Reviews)*, **35**(2), pp. 233–243.

- [35] Deb, K., Pratap, A., Agarwal, S., and Meyarivan, T., 2002, "A Fast and Elitist Multiobjective Genetic Algorithm: NSGA-II," *IEEE Transactions on Evolutionary Computation*, **6**(2), pp. 182–197.
- [36] Deb, K., and Sundar, J., 2006, "Reference Point Based Multi-Objective Optimization Using Evolutionary Algorithms," *Proceedings of the 8th Annual Conference on Genetic and Evolutionary Computation*, Association for Computing Machinery, New York, NY, USA, pp. 635–642.
- [37] Qingfu Zhang and Hui Li, 2007, "MOEA/D: A Multiobjective Evolutionary Algorithm Based on Decomposition," *IEEE Trans. Evol. Computat.*, **11**(6), pp. 712–731.
- [38] Deb, K., and Jain, H., 2014, "An Evolutionary Many-Objective Optimization Algorithm Using Reference-Point-Based Nondominated Sorting Approach, Part I: Solving Problems With Box Constraints," *IEEE Transactions on Evolutionary Computation*, **18**(4), pp. 577–601.
- [39] "A Unified Evolutionary Optimization Procedure for Single, Multiple, and Many Objectives | IEEE Journals & Magazine | IEEE Xplore" [Online]. Available: <https://ieeexplore.ieee.org/document/7164289>. [Accessed: 30-Jul-2024].
- [40] Vesikar, Y., Deb, K., and Blank, J., 2018, "Reference Point Based NSGA-III for Preferred Solutions," *2018 IEEE Symposium Series on Computational Intelligence (SSCI)*, pp. 1587–1594.
- [41] Barrett, M., and Johnson, P., 2005, "Performance and Mass Modeling Subtleties in Closed-Brayton-Cycle Space Power Systems," *3rd International Energy Conversion Engineering Conference*, American Institute of Aeronautics and Astronautics, San Francisco, California.